Quantitative Evaluation of Hydrogen Effects on Evolutions of Deformation-Induced ε-Martensite and Damage in a High-Mn Steel

CHUNXI HAO, MOTOMICHI KOYAMA, and EIJI AKIYAMA

We investigated the effects of hydrogen on ε-martensite-related damage evolution (crack/void initiation and growth) in Fe-Mn-Si-base austenitic steel using tensile tests after gaseous hydrogen charging at 100 MPa. Specifically, we evaluated the quantitative hydrogen effects on ε-martensite fraction and associated damage evolution with different strains and strain rates. Hydrogen charging increased the probability of ε-martensite-related damage initiation and deteriorated micro-damage arrestability, which decreased elongation. The primary factor causing the detrimental hydrogen effects on resistance to damage evolution was the promotion of deformation-induced γ-ε martensitic transformation. An increasing strain rate from 10^{-4} to 10^{-2} s^{-1} suppressed the γ-ε martensitic transformation and correspondingly increased elongation. Interestingly, the ε-martensite fraction near the fracture surface did not change with increasing strain rate, but the area fraction of the brittle-like fracture region decreased. This fact implied that the brittle-like fracture at the low strain rate, which had a longer time for damage growth, was assisted by stress-driven hydrogen diffusion near the crack/void tips.

© The Minerals, Metals & Materials Society and ASM International 2020

I. INTRODUCTION

DEFORMATION-INDUCED martensitic transformation has been used to improve work hardenability and has been associated with uniform elongation, *i.e.*, the transformation-induced plasticity (TRIP) effect.[1,2] In steels, two types of martensitic transformation have been representatively recognized: transformations from face-centered cubic (γ) to body-centered cubic/tetragonal (α′) structures and to hexagonal close-packed (ε) structures. Both types of martensitic transformation result in the TRIP effect,[3–10] but γ-ε martensitic transformation can cause microstructural damage evolution (here, the damage means voids and cracks in the microstructure scale),[11] and associated premature fracture,[12] depending on the alloying element, microstructure, and deformation conditions such as temperature. Therefore, the use of γ-ε martensitic transformation requires appropriate alloy/microstructure designs to control resistance to damage evolution.

In terms of chemical composition, interstitial elements have a strong effect on the behavior of martensitic transformation. For instance, carbon increases the phase stability of γ, which prevents thermally induced γ-ε martensitic transformation. However, carbon has a promotion effect on martensitic transformation as well: it promotes deformation-induced γ-ε martensitic transformation by preventing dislocation slip through solid solution hardening of the γ phase.[13–15] Similarly, hydrogen, which is another interstitial element in steels, also has multiple roles in martensitic transformation. Specifically, hydrogen reduces stacking fault energy,[16–20] decreases the chemical driving force for the transformation,[21] and suppresses dislocation slip by solution hardening.[22,23] Furthermore, hydrogen accelerates the occurrence of ε-martensite-related cracking, which makes the damage problem serious, *i.e.*, hydrogen embrittlement.[24,25] However, when regarded as hydrogen-resistant steels, the formation of ε-martensite has some advantageous features: (1) the γ/ε interface acts as micro-crack arrest site,[12,26] and (2) ε-martensite is more resistant to hydrogen in terms of fatigue crack growth, compared with α′-martensite.[26–29] Therefore, an optimized hydrogen-damage-transformation relationship may enable new high-strength hydrogen-resistant steels. This point of view makes exploring the hydrogen effect on deformation-induced martensitic transformation more valuable.

CHUNXI HAO is with the Institute for Materials Research, Tohoku University, Katahira 2-1-1, Aoba-ku, Sendai, Miyagi, 980-8577, Japan and also with the School of Science, Xi'an Jiaotong University, Xi'an 710049, P.R. China. MOTOMICHI KOYAMA is with the Institute for Materials Research, Tohoku University and also with the Elements Strategy Initiative for Structural Materials (ESISM), Kyoto University, Yoshida-honmachi, Sakyo-ku, Kyoto 606-8501, Japan. Contact e-mail: koyama@imr.tohoku.ac.jp EIJI AKIYAMA is with the Institute for Materials Research, Tohoku University.

To utilize γ-ε martensitic transformation to develop hydrogen-resistant steels, we must first understand the intrinsic effects of hydrogen on microstructure and damage evolution. In this study, we note the effects of hydrogen on deformation-induced ε-martensite fraction and ε-martensite-related damage evolution. In particular, the damage evolution is analyzed in terms of damage initiation probability, damage arrestability, and damage morphology. Then, we present how the hydrogen-dependent transformation behavior is significant regarding microstructural damage evolution and the associated fracture behavior.

II. EXPERIMENTAL PROCEDURES

A. *Materials*

An ingot with a nominal composition of Fe-29Mn-7Cr-6Si in mass pct was prepared by induction melting. The ingot was forged and hot rolled at 1273 K. The rolled bar was homogenized at 1473 K for 2 hours. It was then annealed at 1273 K for 1 hour in air and subsequently water quenched. The detailed chemical composition is shown in Table I. Figure 1 shows the microstructure after annealing, which indicates no martensite forms in the as-annealed condition. The average grain size was 69 μm including the annealing twin boundaries. Specimens were taken from the annealed bar by spark machining. The Fe-29Mn-7Cr-6Si alloy has been reported to show deformation-induced γ-ε martensitic transformation at ambient temperature.[30]

B. *Hydrogen Charging and Tensile Tests*

Hydrogen was introduced into the specimens by hydrogen gas charging at 100 MPa at 543 K for 238 hours. The hydrogen content was measured by thermal desorption spectroscopy (TDS) from room temperature to 995 K at a heating rate of 400 K h^{-1}. The hydrogen-charged specimens were preserved in a refrigerator at 186 K until the TDS measurements were conducted. The cooling to 186 K may induce thermally induced martensitic transformation, which alters the TDS profile. Therefore, the TDS datum was used only for determining diffusible hydrogen content that corresponds to an amount of hydrogen mainly located at interstitial lattice, vacancy, dislocation, and grain boundary. The hydrogen content was determined as cumulative desorbed hydrogen content from room temperature to 995 K.

Tensile specimens with gauge dimensions of 4 mm in width, 1 mm in thickness, and 30 mm in length (Figure 2) were taken along the rolling direction (RD) using electric discharged machining. The specimens were electrochemically polished before the tensile testing. The tensile tests were conducted at initial strain rates of 1×10^{-4} and 1×10^{-2} s^{-1} and at ambient temperature. The strains were measured using a video extensometer.

C. *Microstructure and Damage Characterizations*

Microstructure observations were performed using a scanning electron microscope (SEM). Specifically, martensite distribution and fraction were characterized by electron back scattering diffraction (EBSD) measurements. The martensite fraction was quantified by using area fraction of regions indexed as ε-martensite by the EBSD measurements. The microstructures surrounding the damage were observed by electron channeling contrast imaging (ECCI). The specimens for the microstructure observations were prepared by mechanical polishing with grinding papers, 3 and 9 μm diamond slurry, and colloidal silica with a particle size of 60 nm. The ECCI was conducted at 20 kV. The EBSD analysis was operated at 20 kV with a beam step size of 0.2 μm or 50 nm. The fracture surfaces were also observed by SEM.

Deformation-induced damages such as cracks and voids were quantified in terms of the damage area fraction, which is defined as A_d/A_a, where A_d is the damage area and A_a is the area of the entire region observed. Because cracks and voids appear as black in the SEM micrographs, the damage area was measured from digitized scanning electron micrographs taken of various local plastic strains. Various plastic strains were obtained in a single fractured specimen, that is, the highest strain was obtained beneath the fracture surface, and the strain decreased with increasing distance from the fracture surface. Accordingly, the damage area fraction was measured at several different locations in the single fracture specimen.[31,32] The local tensile plastic strain, ε_{xx}, for each observation region was determined from the local reduction in thickness, which is defined as

$$\varepsilon_{xx} = \ln\left(\frac{t_0}{t}\right) \quad [1]$$

where t_0 and t are the initial thickness and local thickness of the observation region, respectively. The local thickness of the observation region was measured using SEM micrographs. In addition, the number of damages per area was also measured from the same images. Then, average damage size (d_{ave}) was calculated from another two values: $d_{ave} = D_a/n$, where D_a is the damage area fraction, and n is the number of damage incidents per area.[31,33] In addition, the minimum damage size used for the damage quantification was 0.11 μm^2.

III. RESULTS

A. *Hydrogen Effects on Tensile Behavior*

Figure 3 shows the TDS profile of the hydrogen-charged specimen without deformation. Only a single peak was observed, and the hydrogen content was measured to be 27.1 mass ppm (1421 appm). The hydrogen content is lower than that in typical 300-series austenitic stainless steels and other face-centered cubic structure metals (*e.g.*, > 80 mass ppm for 300-series

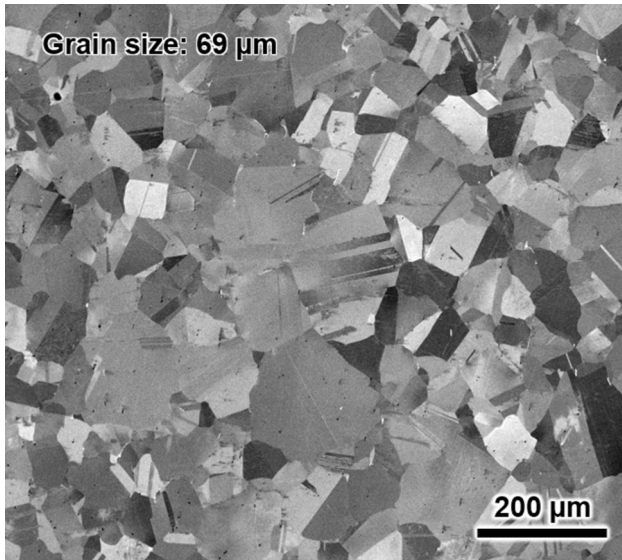| Alloy	Mn	Cr	Si	S	P	O	N	Fe
Fe-29Mn-7Cr-6Si	28.84	7.04	6.14	0.01	< 0.002	0.007	0.031	bal.

Fig. 1—Electron channeling contrast image that shows the microstructure after annealing.
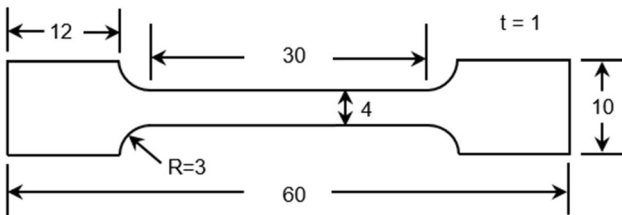
Fig. 2—Specimen dimensions for tensile testing (unit: mm).
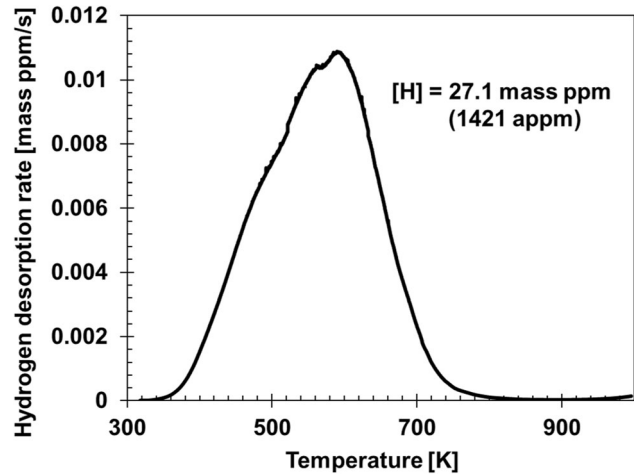

Fig. 3—Hydrogen desorption rate plotted against temperature in hydrogen-charged specimen.
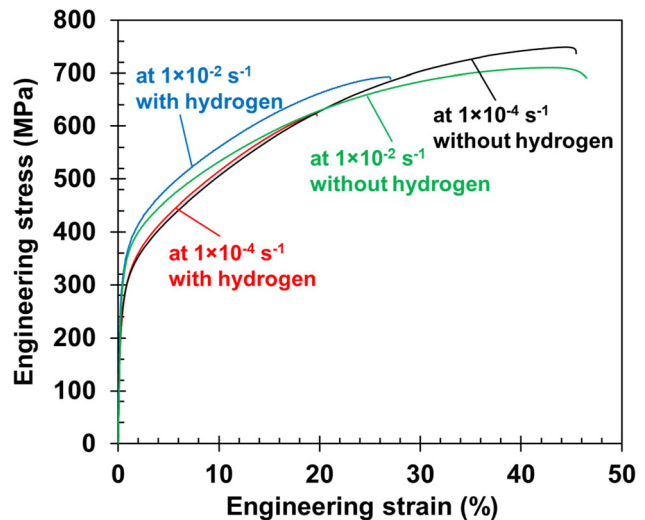
Fig. 4—Tensile behavior of the specimens with and without hydrogen charging at different strain rates.

austenitic stainless steels,[34,35] >100 mass ppm for an equiatomic CoCrFeMnNi alloy,[36] and > 50 mass ppm for pure Ni[37]). A possible reason is the presence of high-concentration Si (6 mass pct), because Si has been reported to prevent hydrogen uptake or decrease hydrogen solubility in austenitic steels.[25,38]

Figure 4 shows the engineering stress-engineering strain curves of the specimens with and without hydrogen charging at different strain rates at room temperature. The hydrogen charging deteriorated the elongation at a strain rate of 10^{-4} s^{-1}. The elongation of the hydrogen-charged specimen at 10^{-2} s^{-1} was also lower than that in the uncharged specimen with the identical strain rate. However, the degree of hydrogen-induced deterioration of elongation at 10^{-2} s^{-1} was slightly lower than that at 10^{-4} s^{-1}. Furthermore, the hydrogen charging increased the flow stress, irrespective

of strain rate. For instance, the 10 pct flow stress at 10^{-4} s^{-1} the slightly increased from 516 to 525 MPa by hydrogen charging.

B. Damage Evolution

Figures 5(a) through (c) show cross-sectional images of the fractured specimens, and the black portions of the images have been identified as damage. By comparing the

three images, the number of relatively large damage was confirmed to increase by hydrogen charging (the large damages were indicated by arrows in Figure 5). Specifically, damage shape of the hydrogen-charged specimens appeared to be long and sharp compared with the uncharged specimen. This indicates that crack tip blunting was difficult to occur in the hydrogen-charged specimens compared with that in the uncharged specimen.

For a more detailed characterization of the damage, the deformation-induced damage evolution was quantified in terms of the damage area fraction, the number of damage incidents per area, and the average damage size, as shown in Figure 6. The damage area fraction (Figure 6(a)) and the number of damage incidents per area (Figure 6(b)) were increased by hydrogen charging, irrespective of strain level. Furthermore, Figures 6(a) and (b) indicate that the decreasing strain rate to 10^{-2} s^{-1} suppressed the strain-induced evolution of the damage area fraction and the number of damage incidents per area. Figure 6(c) shows the average damage size. Similar to other multi-phase steels,[31] the average damage size did not show a monotonic increase against strain for all of the three specimens. That is, the damage evolution, in terms of average damage size, can be separated into three stages: (i) damage incubation; (ii) damage arrest; and (iii) damage growth. According to previous literature,[31,33] damage incubation is defined as the stage before the initiation of the first damage. In the damage arrest stage, the average damage size remains nearly constant with respect to strain. Damage growth indicates the stage after the average damage size begins to increase again. For the uncharged specimen, the end of the damage incubation and arrest steps were at approximately 0.08 and 0.29 strains, respectively. When tested at the strain rate of 10^{-4} s^{-1} after hydrogen charging, the specimen showed the acceleration of the ends of the two regimes, $i.e$, below 0.01 and 0.11 strains for damage incubation and arrest, respectively. The specimen tested at 10^{-2} s^{-1} showed similar critical strains to those of the hydrogen-charged specimen with a strain rate of 10^{-4} s^{-1}.

C. Microstructure Evolution

Figure 7 shows inverse pole figure (IPF) maps of the tensile axis and corresponding phase maps at approximately 0.14 local strain. In comparisons among the images shown in the set in Figure 7, plate-like ε-martensite was observed in all of the specimens, and hydrogen charging increased the fraction of ε-martensite at nearly identical strain. From the phase maps, including Figure 7, the martensite fractions at various strains were quantified as depicted in Figure 8. The hydrogen charging increased the martensite fraction, regardless of strain. Furthermore, the ε-martensite fraction with hydrogen decreased with increasing strain rate but was higher than that without hydrogen charging. Hence, the hydrogen charging and decreasing strain rate promoted deformation-induced γ-ε martensitic transformation in the present steel, irrespective of strain.

Figure 9 shows representative examples of the microstructures surrounding the damage in the uncharged specimen. There are two types of damage initiation sites. The first type of cracking site was the inclusion or inclusion/matrix interface, which is the typical site for damage evolution in general ductile fracture. The other type was ε-martensite-related damage initiation. Corresponding to the EBSD results in Figure 7, the ECC image in Figure 9(a) shows plate-like ε-martensite as a relatively bright contrast. Tiny voids formed within or along the ε-martensite plates. From the tiny voids, sharp cracks formed as indicated by the arrows in Figure 9(a). Then, the damage evolved via the repetition of crack tip blunting and crack/void formation or damage coalescence. The damage evolution process remained even after the damage length reached 50 μm, as shown in Figure 9(b). The damage morphology shown in Figure 9(b) indicates occurrence of the repetition of crack tip blunting and subsequent sharp crack formation at the blunt crack tip.

When hydrogen was introduced, the specimen that was deformed at the strain rate of 10^{-4} s^{-1} showed a larger number of nano-scale voids compared with the uncharged specimen. Nano-voids with a size below 0.1 μm^2, which could be detected in the damage quantification in Figure 6, were also observed (the inset of Figure 10(a)). The initiation sites for the nano-voids were the grain boundary, twin boundary, and within the ε-martensite, as shown in Figures 10(a) and (b). After the damage initiation, the damage grew over the grain size, and the sharpness of the crack tip remained (the ratio of crack length to crack tip opening displacement
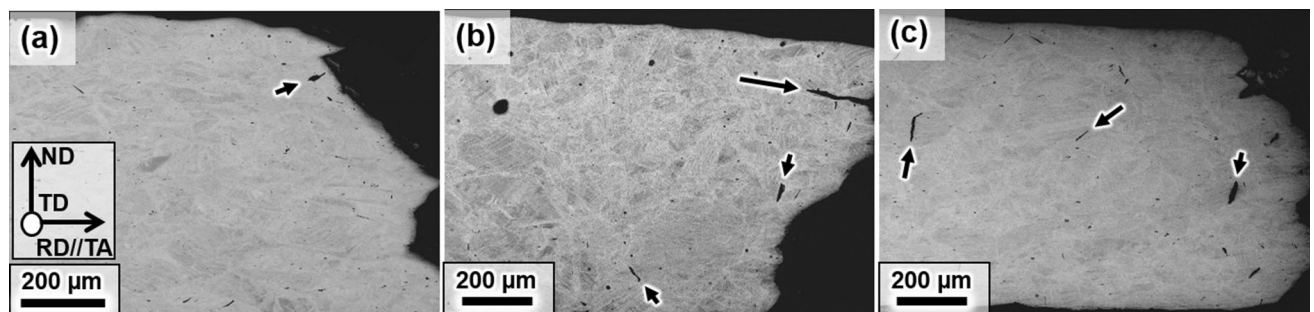

Fig. 5—SEM images showing damage near the fractured surfaces of the specimens (*a*) without hydrogen charging at a strain rate of 1×10^{-4} s^{-1}; (*b*) with hydrogen charging at a strain rate of 1×10^{-4} s^{-1}; and (*c*) with hydrogen charging at the strain rate of 1×10^{-2} s^{-1}. The arrows indicate relatively large cracks. ND, TD, RD, and TA indicate normal direction, transverse direction, rolling direction, and tensile axis, respectively.
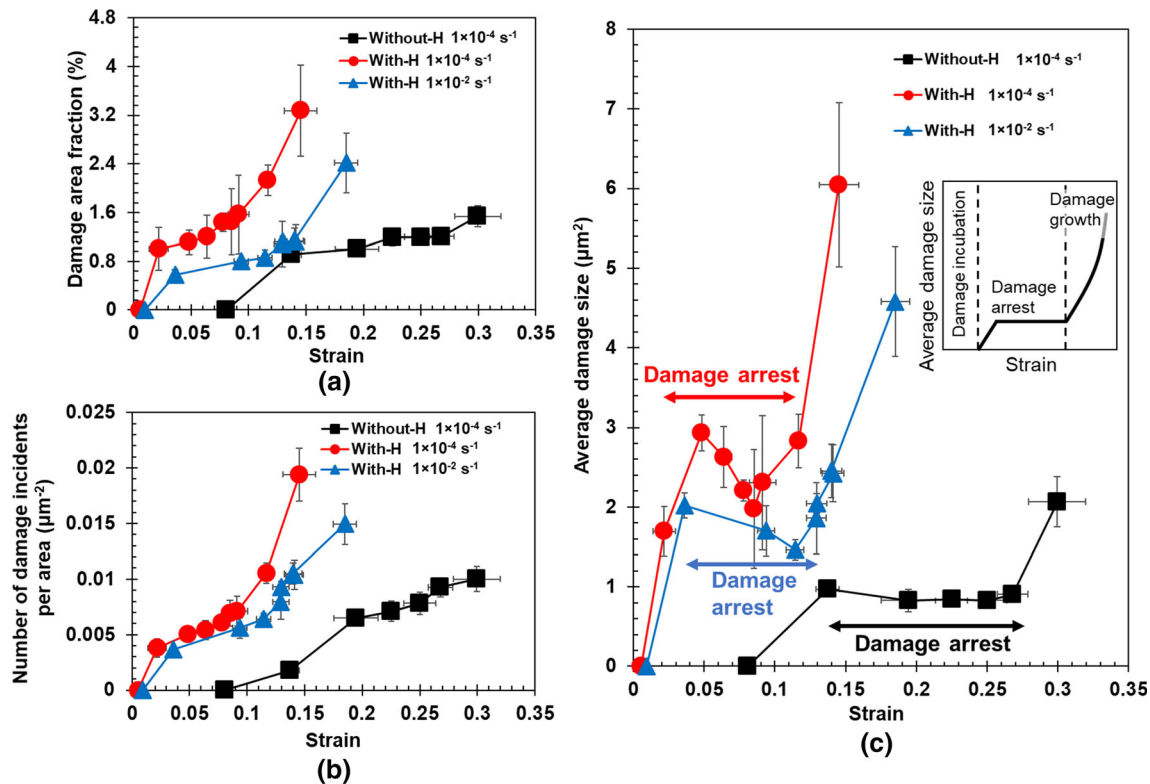
Fig. 6—(a) Damage area fraction, (b) number of damage incidents per area, and (c) average damage size plotted against strain. The inset indicates a schematic illustration that indicates the three damage evolution regimes in the average damage size-strain relationship. The arrows in (c) indicate strain ranges corresponding to the damage arrest stages.

was over 50 unlike void-like damages.) (Figure 10(c)). Furthermore, the damage growth occurred along the fine zigzag path, particularly when the growth path was grain interior. The damage initiation site, morphology and evolution characteristics did not change by increasing the strain rate to 10^{-2} s^{-1} in the hydrogen-charged specimen, as shown in Figure 11(a). Nano-voids along grain boundaries and the zigzag growth of the transgranular damage were also observed (Figures 11(b) and (c)).

D. Fracture Surface

Figure 12 shows fracture surfaces of the three specimens: without hydrogen charging and with a strain rate of 1×10^{-4} s^{-1}, with hydrogen charging and a strain rate of 1×10^{-4} s^{-1}, and with hydrogen charging and a strain rate of 1×10^{-2} s^{-1}. The fracture surface of the uncharged specimen showed dimples as a major feature (Figure 12(a)) and partially quasi-cleavage features (Figure 12(a)). Specifically, step-like ridges were observed on the quasi-cleavage fracture surface. When hydrogen charging was performed, the predominant fractographic feature changed to a brittle-like feature that consisted of quasi-cleavage and intergranular fracture surfaces (Figures 12(b) and (c)). Similar to the uncharged specimen, the quasi-cleavage fracture surface of the hydrogen-charged specimen showed step-like ridges (Figures 12(b) and (c)). It is also noteworthy that the intergranular fracture surface also showed step-like

ridges. The predominant fractographic feature involving the step-like ridges did not change with a strain rate increase from 10^{-4} to 10^{-2} s^{-1}. The area fraction of the brittle-like fracture surface increased with hydrogen charging and decreased with increasing strain rate, as listed in Table II.

IV. DISCUSSION

According to Figure 6(c), the damage evolution in both of the uncharged and hydrogen-charged specimens can be separated into three stages: (i) damage incubation, (ii) damage arrest, and (iii) damage growth, which is similar to those of dual phase steels.[31,40,41] Here, we discuss hydrogen and strain rate effects on the respective stages of the damage evolution in terms of martensitic transformation.

A. Damage Initiation and Arrest

The damage initiation within or along ε-martensite plates has been commonly observed in various Co alloys[42,43] and Fe-Mn alloys[11,12] that showed deformation-induced γ-ε martensitic transformation, even when hydrogen charging was not performed. The damage initiation is attributed to interactions between primary and secondary ε-martensite plates.[44,45] Therefore, the transgranular damage initiation occurs in grains in which ε-martensite plates form along multiple
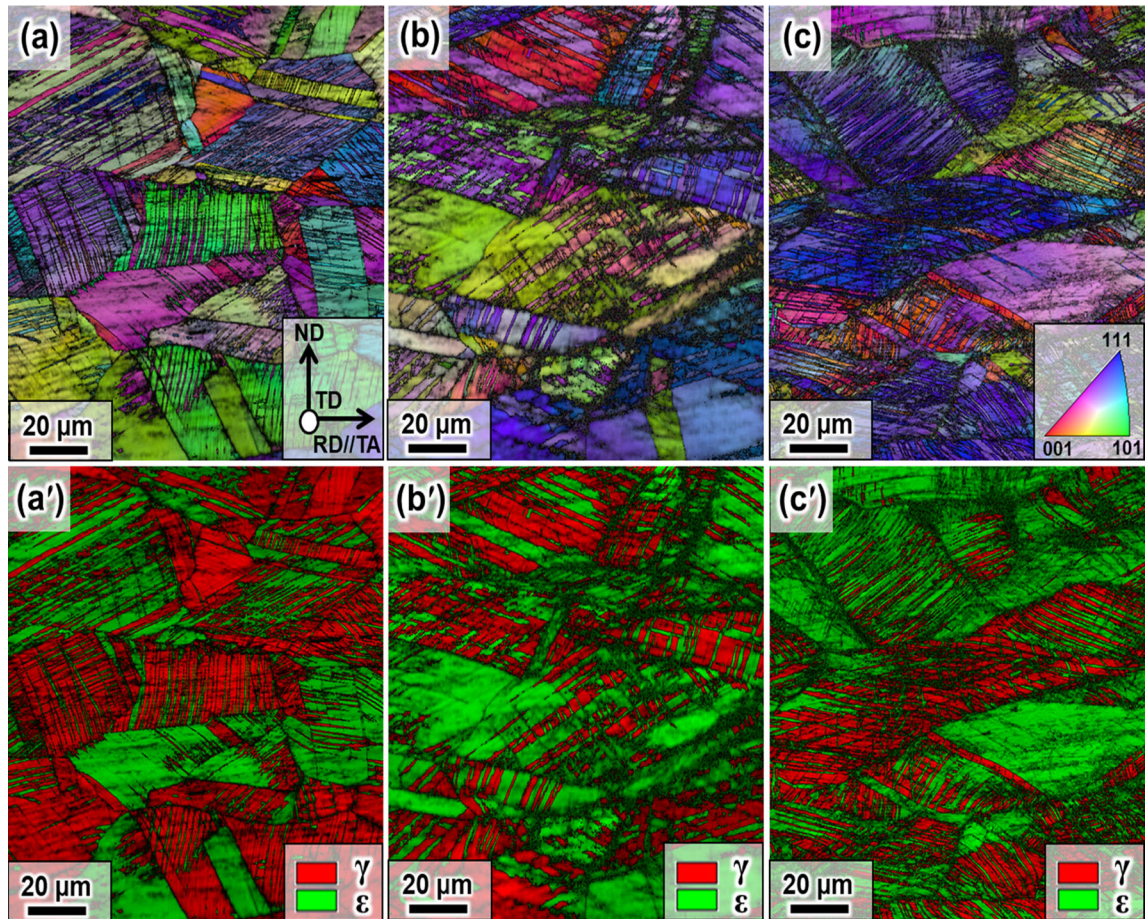
Fig. 7—(a–c) RD-IPF and (a′–c′) phase maps of the three specimens: (a, a′) uncharged specimen with 0.14 strain at a strain rate of 1×10^{-4} s^{-1}; (b, b′) hydrogen-charged specimen with 0.13 strain at a strain rate of 1×10^{-4} s^{-1}; (c, c′) hydrogen-charging specimen with 0.15 strain at a strain rate of 1×10^{-2} s^{-1}. In the phase maps, red and green regions correspond to austenite (γ) and ε-martensite, respectively.

planes, as observed in Figure 9(a). Although direct evidence for the activation of this mechanism could not be obtained, the appearance of the quasi-cleavage fracture surface with step-like ridges, which is seen in Figures 12(a) through (c), is the typical feature indicating the occurrence of damage initiation associated with the interaction of ε-martensite plates.[12] When ε-martensite is ductile like the present steel without hydrogen, damage tip blunting subsequently occurs *via* plastic deformation of the ε-martensite and the remaining austenite region surrounding the damage.[46,47] The damage tip blunting decreases local stress, which temporally reduces the driving force for further damage growth. Although the damage grows through the repetition of damage tip blunting and the formation of sharp damage tips as observed in Figure 9(a), the damage size does not increase to more than the grain size. Therefore, the average damage size shows at steady state until 0.25 strain, although the damage was already initiated at 0.08 (Figure 6(c)). As a result, the damage initiation in the uncharged specimen did not play a critical role in the fracture, which thereby enables necking and ductile fracture as the predominant mode.

From the perspective of damage initiation, hydrogen charging increased the damage initiation probability (Figure 6(b)) and decreased the critical strain for the damage initiation from 0.08 to 0.01 (Figure 6(c)). To discuss the promotion of damage initiation due to hydrogen, we note three possible hydrogen effects: (1) the deterioration of ductility in ε-martensite, (2) the decrease in twin and grain boundary strengths, and (3) the promotion of deformation-induced ε-martensitic transformation. In terms of the first factor, the acceleration of the transgranular damage initiation of ε-martensite due to hydrogen is the key observation factor that indicates the deterioration in ε-martensite ductility. In general, ε-martensite is easy to crack because of the plastic anisotropy of the hexagonal close-packed structure. Therefore, when α-martensite does not form like the present steel, a non-basal slip or twin formation is required for stress accommodation. Because critical resolved shear stress for the unusual deformation mechanism is generally high, a stress-controlled cracking mechanism can occur from slight reduction in the stress accommodation capability. Although the specific effect of hydrogen on the stress accommodation capability in ε-martensite is unclear, the
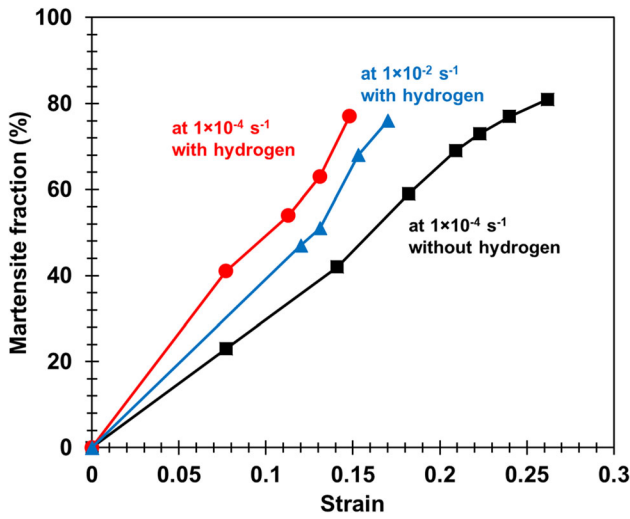
Fig. 8—Hydrogen and strain rate effects on the relationship between the martensite fraction and tensile strain. Data at the true strain of 0.03 at 10^{-4} s^{-1} with and without hydrogen charging were obtained in the previous study.[39]

solution hardening by hydrogen was actually observed in Figure 4. The increase in strength indicates that the stress required to activate the stress accommodation mechanism at the cracking site also increases.

The second factor, a decrease in twin and grain boundary strengths, provides additional damage initiation sites, which simply increases the number of damage incidents. Although there is no experimental evidence for hydrogen-reduced boundary strength, hydrogen has been theoretically clarified to segregate at the grain boundaries of face-centered cubic metals,[48] which can decrease the grain boundary strength significantly, resulting in failure.[49] Hydrogen-reduced grain boundary strength has been recognized as important, particularly in twinning-induced plasticity and transformation-induced plasticity steels, because the twin and martensite plates cause microstructural stress concentration.[26,50] According to previous studies, when ε-martensite growth is impinged at grain boundaries, the stress concentration at the tip of the ε-martensite plate results in intergranular micro-damage.[28,50] Because hydrogen decreases the cohesive energy at grain boundaries, the intergranular damage formation at the
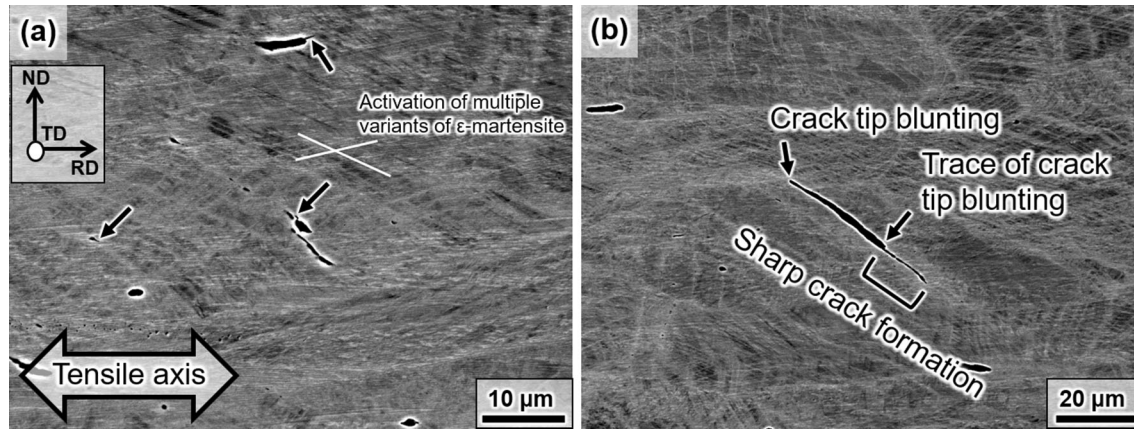

Fig. 9—ECC images showing damage characteristics in uncharged specimens deformed at strain rate of 10^{-4} s^{-1}. (a) A considerable amount of tiny damage formed in the grain where multi-variant ε-martensite was activated. (b) A crack that grew via crack tip blunting and subsequent sharp crack formation. The tensile strain in these regions was 0.23.
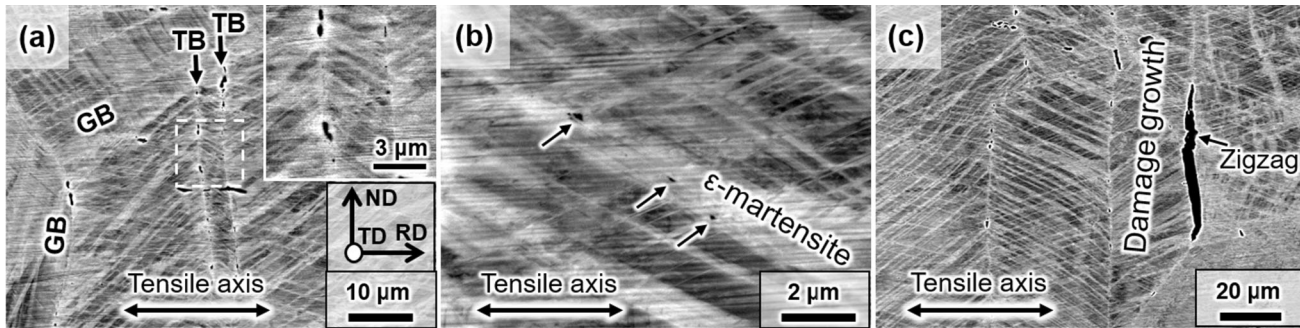

Fig. 10—ECC images of hydrogen-charged specimen deformed at a strain rate of 10^{-4} s^{-1}. Hydrogen-assisted crack initiation at (a) grain and twin boundary and (b) grain interior. (c) Small crack growth. The tensile strain of the region where these images were taken was 0.08. The inset in (a) indicates a magnification of the highlighted region. TB and GB mean twin boundary and grain boundary, respectively. The arrows in (b) indicate damage.
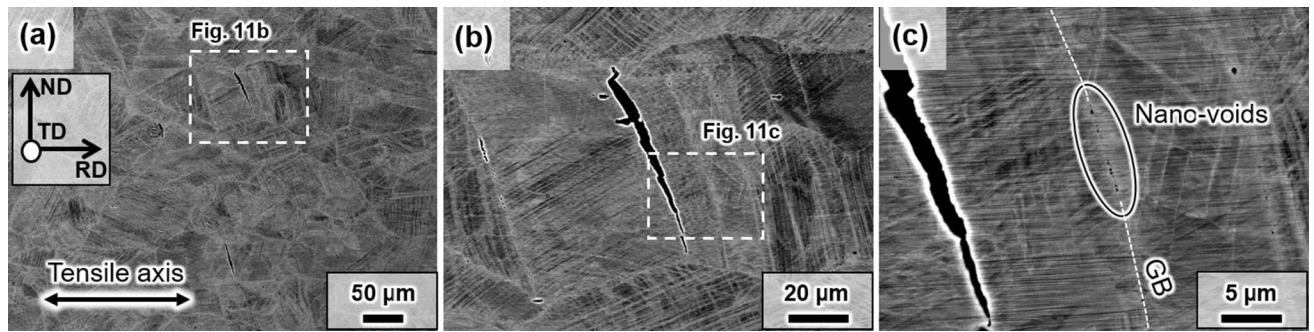
Fig. 11—ECC images with different magnifications taken in hydrogen-charged specimen deformed at a strain rate of 10^{-2} s^{-1}. (a) Overview and (b, c) magnified images of the region where transgranular damage was observed. The tensile strain of this region was 0.12.
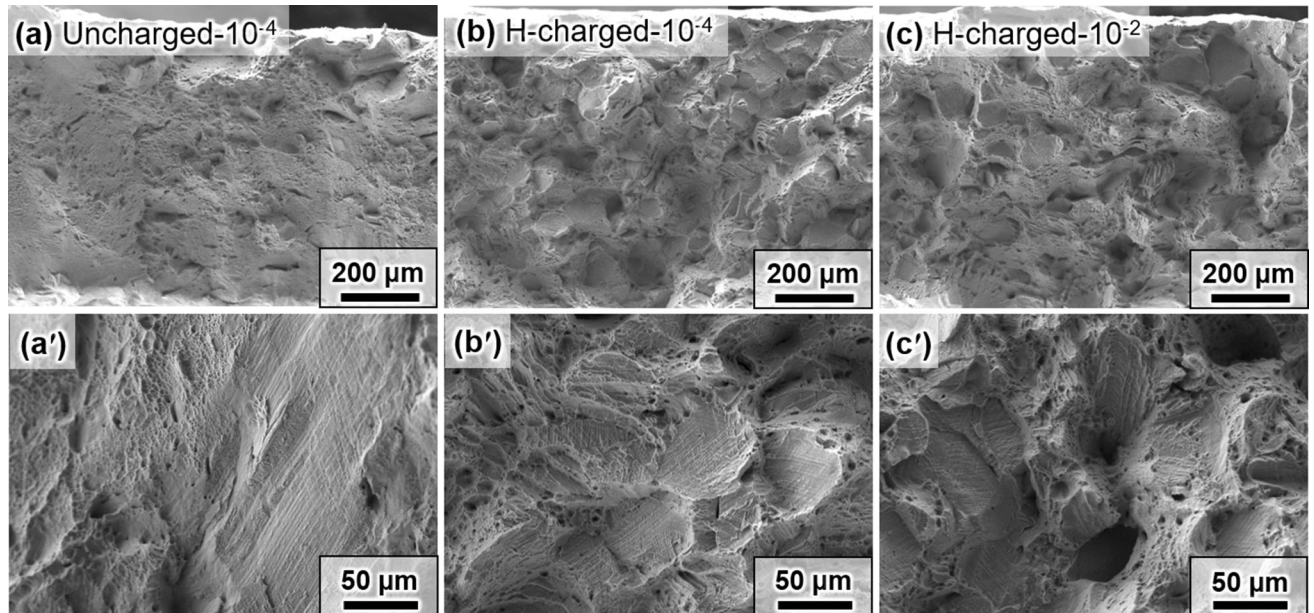

Fig. 12—Fractographs of (a) the uncharged specimen with a strain rate of 1×10^{-4}s^{-1}, (b) hydrogen-charged specimen with a strain rate of 1×10^{-4} s^{-1}, and (c) hydrogen-charged specimen with a strain rate of 1×10^{-2}s^{-1}. (a-c) Magnified fractographs of the respective specimens for (a-c).

ε-martensite plate tips can also be promoted by hydrogen. In contrast, most ε-martensite penetrates the twin boundary *via* the dislocation dissociation of leading partials at the coherent interface.[51,52] However, it has been reported that ε-martensite does not have a shearable crystallographic plane parallel to the crossed twin boundary.[53] In addition, shear on the twin boundary is indispensably required for dislocation dissociation[54–57], *e.g.*,

$$3 \times \frac{1}{6}\left[\bar{1}12\right]\left(\bar{1}1\bar{1}\right) \rightarrow 3 \times \frac{1}{18}\left[\bar{5}52\right](11\bar{5}) + 2 \times \frac{1}{6}\left[1\bar{1}2\right]\left(\bar{1}11\right) \qquad [2]$$

where $1/6\left[\bar{1}12\right]$ is the Burgers vector of the incident leading partial, the $\left(\bar{1}11\right)$ plane is the crossed twin boundary, and $1/18\left[\bar{5}52\right](11\bar{5})$ corresponds to $1/6[112]$ in the twin grain. Namely, $2 \times 1/6\left[1\bar{1}2\right]\left(\bar{1}11\right)$ is the required shear component for the twin boundary. The combination of the two factors causes stress concentration along the twin boundary when the capability of plastic stress accommodation is deteriorated; coupling the geometric effect of the twin boundary and ε-martensite with factors (1) and (2) results in micro-damage. Accordingly, a considerable number of damage incidents were observed, as seen in Figures 10(a) and 11(c).

The third factor, the promotion of deformation-induced ε-martensitic transformation, was experimentally confirmed in Figure 8, which is consistent with the previous study.[22] The possible reasons for the promotion of ε-martensitic transformation by hydrogen can be attributed to (1) the suppression of the dislocation slip by solution hardening,[16] (2) a decrease in the stacking fault energy,[58] and (3) a reduction in the repulsive stress between dislocations that facilitates dislocation core

Table II. Area Fraction of Brittle-Like Fracture Surface Region

Specimen	Uncharged-Tensile Test Rate 10^{-4} s^{-1}	H-Charged-Tensile Test Rate 10^{-4} s^{-1}	H-Charged-Tensile Test Rate 10^{-2} s^{-1}
Area Fraction of Brittle-Like Fracture Surface Region (Pct)	12	91	75

restructuring for nucleation.[59] Hydrogen has been reported to enhance all these factors in austenitic steels. Hydrogen-assisted ε-martensitic transformation increases the probability of damage initiation along or within the ε-martensite plate. Simultaneously, the promotion of ε-martensitic transformation increases the probability of its interactions with the grain and twin boundaries. Therefore, the third factor plays a detrimental role in the damage initiation probability. The hydrogen effect on the ε-martensite fraction showed negative strain rate dependence (Figure 8), which corresponds to the deterioration of damage initiation resistance (Figure 6(b)). The negative strain rate dependence of the ε-martensite fraction can be explained by the effects of hydrogen-decorated dislocation motion.[60,61] The mobility of transformation dislocation can be enhanced by decreasing the strain rate, particularly when hydrogen is introduced, because the competitive motion of dislocations and diffusible hydrogen occurs, which leads to an increase in the deformation-induced martensite fraction. Because the hydrogen-assisted ε-martensitic transformation plays multiple roles in damage initiation, the strain-rate-sensitive ε-martensite fraction can play the primary role in the strain rate dependence of the hydrogen embrittlement behavior in the present steel.

B. Damage Growth and Fracture

As seen in Figure 6(c), the hydrogen charging not only deteriorated damage initiation resistance, but also damaged arrestability. To consider the predominant damage growth path, we must note the fractographic features. The brittle-like fracture surface involving the step-like ridges is a typical characteristic when ε-martensite contributes to the fracture.[12] Specifically, ε-martensite plates interacting with another ε-martensite, grain boundary, and twin boundary cause tunnel-like nanovoids, and subsequent damage growth via their coalescence leaves step-like ridges on the fracture surface.[12,62] The ε-martensite-related damage initiation did not act as the primary factor triggering the final failure in the uncharged specimen because the area fraction of the brittle-like fracture surface region was only 12 pct, as listed in Table II. Most of the ε-martensite-related damage was fully arrested after its growth to the grain size scale. However, the area fraction of the brittle-like fracture surface region of the hydrogen-charged specimen tested at the strain rate of 10^{-4} s^{-1} was 91 pct, and entire region of the brittle-like fracture surface involved step-like ridges. These facts indicate that the hydrogen-assisted damage growth at the strain rate of 10^{-4} s^{-1}

is attributed to the coalescence of tunnel-like ε-martensite-related damage.

It can be considered that resistance to damage coalescence is predominantly dependent on four factors: (1) the ε-martensite fraction at the damage tip, which increases the microstructural stress concentration and probability of new damage initiation during damage tip opening (Figure 13(a)),[11] (2) the number of pre-existing damage incidents on the damage growth path (Figure 13(b)),[63] (3) the cohesive energy at the weakest interface in the ligaments between damage points (Figure 13(c)),[62] and (4) the plastic shear resistance of the ligaments (Figure 13(d)).[64] Similar to the damage initiation, hydrogen promoted deformation-induced ε-martensitic transformation in the late stage of the deformation, and numerous ε-martensite plates were observed near the damage tips. Therefore, the first factor is intrinsically important in understanding the deterioration of the damage arrestability due to hydrogen. The promotion of ε-martensitic transformation is directly related to the damage initiation probability, as discussed in the Section IV–A. Accordingly, the number of damage points, i.e., the second factor, reached more than double at the same strain by hydrogen charging, as shown in Figure 6(b). Furthermore, a considerable number of very tiny points of damage, which were not counted in Figure 6(b), were also observed in the hydrogen-charged specimens after significant plastic deformation (Figures 10(a) and (b)). Because most of the observed damage was placed at the ε-martensite, grain boundary, and twin boundaries that were primary damage growth paths, the pre-existing damage reduces the damage growth resistance (Figure 13(b)).

However, it is also noteworthy that the ε-martensite fraction near the fracture surface was almost the same between the hydrogen-charged specimens tested at 10^{-4} and 10^{-2} s^{-1} (Figure 8), and the area fraction of the brittle-like fracture surface region decreased with increasing strain rate (Table II). Even with the same amount of ε-martensite, the damage growth path and associated damage arrestability can change as a result of other time-dependent hydrogen-related factors. Considering the third factor, when the shape of the damage tips is sharp, a significant hydrostatic stress gradient forms, which accelerates the hydrogen segregation at the tips (Figure 13(c)). The hydrogen segregation may assist with damage coalescence via hydrogen-enhanced decohesion. The fourth factor is significant in austenitic steels, particularly when the dislocation planarity is high and the spacing of damage incidents is narrow.[64] Possible roles of hydrogen that assist in plastic shear are hydrogen-enhanced localized plasticity[65,66] and
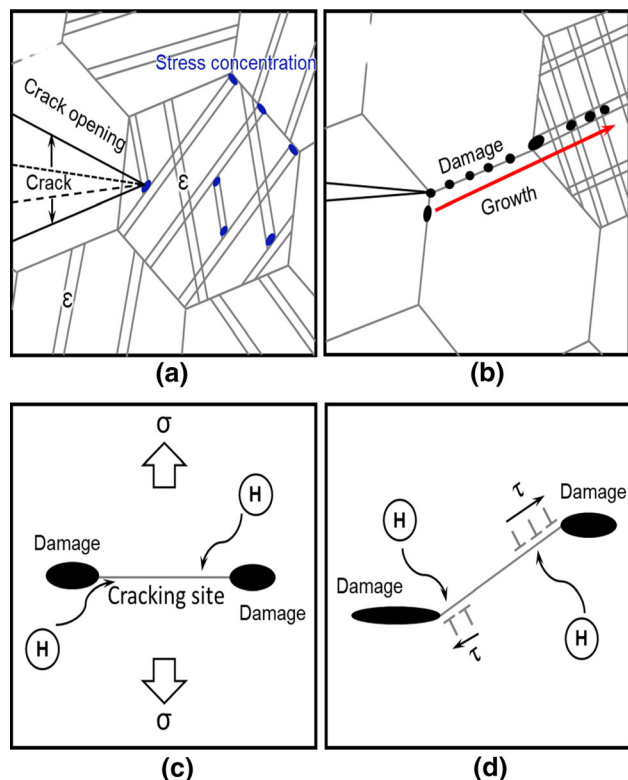
Fig. 13—Schematic of four factors for which the resistance to damage coalescence is predominantly (*a*) ε-martensite fraction at the damage tip, (*b*) number of pre-existing points of damage on the damage growth path, (*c*) cohesive energy at the weakest interface in ligaments between points of damage, and (*d*) plastic shear resistance of the ligaments.

hydrogen-enhanced dislocation emission from a damage tip.[67] The former hydrogen effect softens the ligament material of the damage, for which the degree is enhanced with decreasing strain rate because the hydrogen motion is required to be comparable to the dislocation velocity.[65,66,68] The latter assists with damage tip deformation, for which the effect also has a significant strain rate dependence due to the hydrogen segregation at the damage tip.[67,69] The combination of these factors is key to interpreting the strain-rate-dependent effect of hydrogen on ε-martensite-related damage growth.

V. CONCLUSIONS

We observed the effects of hydrogen on the strain dependence of ε-martensite fraction and damage evolution in Fe-Mn-Si-base austenitic steel. The results show that hydrogen pre-charging and strain rate play key roles in ε-martensite-related damage evolution. The main conclusions are given below.

1. Hydrogen charging deteriorated elongation, which was associated with ε-martensite-related damage evolution. From the perspective of damage initiation, hydrogen charging increased the damage initiation probability and decreased the critical strain for the damage initiation from 0.08 (without hydrogen pre-charging) to 0.01 (with hydrogen pre-charging). To interpret the promotion of damage initiation by hydrogen, we note the three hydrogen effects: (I) the deterioration of ductility in ε-martensite, (II) the decreases in twin and grain boundary strengths that act as additional damage initiation sites, and (III) the promotion of deformation-induced ε-martensitic transformation. According to our observations, the promotion of ε-martensitic transformation by hydrogen was actually significant even at an early deformation stage (low strain level).

2. The hydrogen charging not only deteriorated the damage initiation resistance but also deteriorated damage arrestability. Hydrogen also promoted ε-martensitic transformation at a late stage of plastic deformation. The promotion of ε-martensitic transformation, coupled with other hydrogen embrittlement factors, resulted in the deterioration of damage arrestability.

3. In terms of strain rate, elongation with hydrogen at 10^{-2} s^{-1} was higher than that at 10^{-4} s^{-1}. Interestingly, the ε-martensite fraction near the fracture surface was almost the same between the hydrogen-charged specimens tested at 10^{-4} and 10^{-2} s^{-1}. However, the area fraction of the brittle-like fracture surface region decreased with increased strain rate. As a result, even with the same amount of ε-martensite, the damage growth path and associated damage arrestability can change because of other time-dependent hydrogen-related factors such as hydrogen diffusion to the damage tips.

REFERENCES

1. V.F. Zackay, E.R. Parker, D. Fahr, and R. Busch: *Trans. ASM*, 1967, vol. 60, pp. 252–59.
2. I. Tamura: *Met. Sci.*, 1982, vol. 16, pp. 245–53.
3. L. Remy and A. Pineau: *Mat. Sci. Eng.*, 1977, vol. 28, pp. 99–107.
4. K. Sipos, L. Remy, and A. Pineau: *Met. Trans. A*, 1976, vol. 7, pp. 857–64.
5. M. Koyama, T. Sawaguchi, and K. Tsuzaki: *Mater. Trans.*, 2015, vol. 56, pp. 819–25.
6. O. Grässel and G. Frommeyer: *Mater. Sci. Technol.*, 1998, vol. 14, pp. 1213–17.
7. S. Kang, Y.S. Jung, J.H. Jun, and Y.K. Lee: *Mater. Sci. Eng. A*, 2010, vol. 527, pp. 745–51.
8. T. Niendorf, F. Rubitschek, H.J. Maier, J. Niendorf, H.A. Richard, and A. Frehn: *Mater. Sci. Eng.*, 2010, vol. 527, pp. 2412–17.
9. L. Bracke, L. Kestens, and J. Penning: *Scripta Mater.*, 2007, vol. 57, pp. 385–88.
10. G.R. Chanani, V.F. Zackay, and E.R. Parker: *Metall. Trans.*, 1971, vol. 2, pp. 133–39.
11. T. Kaneko, M. Koyama, T. Fujisawa, and K. Tsuzaki: *ISIJ. Int.*, 2016, vol. 56, pp. 2037–46.

12. S. Takaki, T. Furuya, and Y. Tokunaga: *ISIJ. Int.*, 1990, vol. 30, pp. 632–38.
13. Z. Li, C.C. Tasan, H. Springer, B. Gault, and D. Raabe: *Sci. Rep.*, 2017, vol. 7, pp. 40704–1–7.
14. J.B. Seol, J. Jung, Y. Jang, and C. Park: *Acta Mater.*, 2013, vol. 61, pp. 558–78.
15. M. Huang, O. Bouaziz, D. Barbier, and S. Allain: *J. Mater. Sci.*, 2011, vol. 46, pp. 7410–14.
16. A.E. Pontini and J.D. Hermida: *Scripta Mater.*, 1997, vol. 37, pp. 1831–37.
17. M.B. Whiteman and A.R. Troiano: *Phys. Stat. Sol.*, 1964, vol. 7, pp. 109–10.
18. D.P. Abraham and C.J. Altstetter: *Metall. Mater. Trans. A*, 1995, vol. 26, pp. 2859–71.
19. S. Jani, M. Marek, R.F. Hochman, and E.I. Meletis: *Metall. Trans. A*, 1991, vol. 22, pp. 1453–61.
20. A.W. Thompson: *Mat. Sci. Eng.*, 1980, vol. 43, pp. 41–46.
21. Y. Kuroki, S. Kawano, S. Iikubo, H. Ohtani, M. Koyama, and K. Tsuzaki: *Metall. Mater. Trans. A*, 2019, vol. 50, pp. 3019–23.
22. M. Koyama, N. Terao, and K. Tsuzaki: *Mater. Lett.*, 2019, vol. 249, pp. 197–200.
23. E.G. Astafurova, G.G. Zakharova, and H.J. Maier: *Scripta Mater.*, 2010, vol. 63, pp. 1189–92.
24. Y.S. Chun, J.S. Kim, K.-T. Park, Y.-K. Lee, and C.S. Lee: *Mat. Sci. Eng. A*, 2012, vol. 533, pp. 87–95.
25. S.-M. Lee, I.-J. Park, J.-G. Jung, and Y.-K. Lee: *Acta Mater.*, 2016, vol. 103, pp. 264–72.
26. M. Koyama, S. Okazaki, T. Sawaguchi, and K. Tsuzaki: *Metall. Mater. Trans. A*, 2016, vol. 47A, pp. 2656–73.
27. T.C. Chen, S.T. Chen, and L.W. Tsay: *Int. J. Hydrog. Energy*, 2014, vol. 39, pp. 10293–10302.
28. M. Koyama, E. Akiyama, Y.K. Lee, D. Raabe, and K. Tsuzaki: *Int. J. Hydrog. Energy*, 2017, vol. 42, pp. 12706–23.
29. K. Tsuzaki, K. Fukuda, M. Koyama, and H. Matsunaga: *Scripta Mater.*, 2016, vol. 113, pp. 6–9.
30. H. Otsuka, H. Yamada, T. Maruyama, H. Tanahashi, S. Matsuda, and M. Murakami: *ISIJ. Int.*, 1990, vol. 30, pp. 674–79.
31. M. Koyama, C.C. Tasan, E. Akiyama, K. Tsuzaki, and D. Raabe: *Acta Mater.*, 2014, vol. 70, pp. 174–87.
32. C.C. Tasan, J.P.M. Hoefnagels, and M.G.D. Geers: *Acta Mater.*, 2012, vol. 60, pp. 3581–89.
33. M. Koyama, C.C. Tasan, T. Nagashima, E. Akiyama, D. Raabe, and K. Tsuzaki: *Phil. Mag. Lett.*, 2016, vol. 96, pp. 9–18.
34. Y. Murakami, T. Kanezaki, and Y. Mine: *Metall. Mater. Trans. A*, 2010, vol. 41A, pp. 2548–62.
35. Y. Ogawa, S. Okazaki, O. Takakuwa, and H. Matsunaga: *Scripta Mater.*, 2018, vol. 157 (2018), pp. 95–99.
36. M. Koyama, K. Ichii, and K. Tsuzaki: *Int. J. Hydrog. Energy*, 2019, vol. 44, pp. 17163–67.
37. K. Wada, J. Yamabe, and H. Matsunaga: *Materialia*, 2019, vol. 8, p. 100478.
38. K. Yamada, M. Koyama, T. Kaneko, and K. Tsuzaki: *Scripta Mater.*, 2015, vol. 105, pp. 54–57.
39. M. Koyama, C.X. Hao, E. Akiyama, and K. Tsuzaki: *Metall. Mater. Trans. A*, 2020, vol. 51, pp. 4439–41.
40. T. Kumamoto, M. Koyama, K. Sato, and K. Tsuzaki: *Mater. Trans.*, 2019, vol. 60, pp. 2368–77.
41. T. Kumamoto, M. Koyama, K. Sato, and K. Tsuzaki: *Eng. Fract. Mech.*, 2019, vol. 216, p. 106513.
42. M. Vollmer, P. Krooß, C. Segel, A. Weidner, A. Paulsen, J. Frenzel, M. Schaper, G. Eggeler, H.J. Maier, and T. Niendorf: *J. Alloy. Compd.*, 2015, vol. 633, pp. 288–95.
43. K. Prusik, H. Morawiec, B. Kostrubiec, M. Prewendowski, G. Dercz, and K. Ziewiec: *Eur. Phys. J. Spec. Top.*, 2008, vol. 158, pp. 155–59.
44. H. Li, M. Koyama, T. Sawaguchi, K. Tsuzaki, and H. Noguchi: *Phil. Mag. Lett.*, 2015, vol. 95, pp. 303–11.
45. M. Koyama, T. Sawaguchi, and K. Tsuzaki: *Metall. Mater. Trans. A*, 2012, vol. 43, pp. 4063–74.
46. S. Aoki, K. Kishimoto, and N. Takeuchi: *Int. J. Fracture*, 1992, vol. 55, pp. 363–74.
47. V. Tvergaard: *J. Mech. Phys. Solids*, 2004, vol. 52, pp. 2149–66.
48. Y.A. Du, L. Ismer, J. Rogal, T. Hickel, J. Neugebauer, and R. Drautz: *Phys. Rev. B*, 2011, vol. 84, p. 144121.
49. M. Yamaguchi, K.-I. Ebihara, M. Itakura, T. Kadoyoshi, T. Suzudo, and H. Kaburaki: *Metall. Mater. Trans. A*, 2011, vol. 42, pp. 330–39.
50. M. Koyama, E. Akiyama, K. Tsuzaki, and D. Raabe: *Acta Mater.*, 2013, vol. 61, pp. 4607–18.
51. A. Sato, K. Soma, and T. Mori: *Acta Metall.*, 1982, vol. 30, pp. 1901–07.
52. Y.-B. Ju, M. Koyama, T. Sawaguchi, K. Tsuzaki, and H. Noguchi: *Acta Mater.*, 2016, vol. 112, pp. 326–36.
53. T. Maki: *Phase Transformations in Steels*, 1st ed., Woodhead Publishing, Cambridge, 2012, pp. 34–58.
54. J.W. Christian and S. Mahajan: *Prog. Mater. Sci.*, 1995, vol. 39, pp. 1–157.
55. S. Mahajan and G. Chin: *Acta Metall.*, 1973, vol. 21, pp. 173–79.
56. L. Remy: *Acta Metall.*, 1977, vol. 25, pp. 711–14.
57. L. Remy: *Metall. Trans. A*, 1981, vol. 12, pp. 387–408.
58. M. Koyama, K. Hirata, Y. Abe, A. Mitsuda, S. Iikubo, and K. Tsuzaki: *Sci. Rep.*, 2018, vol. 8, p. 16136.
59. P.J. Ferreira, I.M. Robertson, and H.K. Birnbaum: *Acta Mater.*, 1998, vol. 46, pp. 1749–57.
60. J. Tien, A.W. Thompson, I.M. Bernstein, and R.J. Richards: *Metall. Trans. A*, 1976, vol. 7, pp. 821–29.
61. M. Dadfarnia, M.L. Martin, A. Nagao, P. Sofronis, and I.M. Robertson: *J. Mech. Phys. Solids*, 2015, vol. 78, pp. 511–25.
62. B. Bal, M. Koyama, G. Gerstein, H.J. Maier, and K. Tsuzaki: *Int. J. Hydrogen Energy*, 2016, vol. 41, pp. 15362–72.
63. M. Koyama, Y. Onishi, and H. Noguchi: *Int. J. Fracture*, 2017, vol. 206, pp. 123–30.
64. V.K. Verma, M. Koyama, S. Hamada, and E. Akiyama: *Mater. Sci. Eng. A*, 2020, vol. 782, p. 139250.
65. P. Sofronis, Y. Liang, and N. Aravas: *Eur. J. Mech. A-Solids*, 2001, vol. 20, pp. 857–72.
66. I.M. Robertson, P. Sofronis, A. Nagao, M.L. Martin, S. Wang, D.W. Gross, and K.E. Nygren: *Metall. Mater. Trans. A*, 2015, vol. 46, pp. 2323–41.
67. C. Zheng, B. Lv, F. Zhang, Z. Yan, R. Dan, and L. Qian: *Mater. Sci. Eng. A*, 2012, vol. 547, pp. 99–103.
68. M. Koyama, E. Akiyama, and K. Tsuzaki: *Scripta Mater.*, 2012, vol. 66, pp. 947–50.
69. B.A. Kehler and J.R. Scully: *Corrosion*, 2008, vol. 64, pp. 465–77.